$Ba_{2-x}Bi_xCoRuO_6$ ($0.0 \leq x \leq 0.6$) Hexagonal Double Perovskite-Type Oxides as Promising *p*-Type Thermoelectric Materials

Uzma Hira[a, b*], Jan-Willem G. Bos [c], Alexander Missyul[d], François Fauth[d], Nini Pryds[e] and Falak Sher[a*]

[a]Department of Chemistry and Chemical Engineering, Syed Babar Ali School of Science and Engineering, Lahore University of Management Sciences (LUMS), 54792, Lahore, Pakistan

[b]School of Physical Sciences (SPS), University of the Punjab, New Campus, 54590, Lahore, Pakistan

[c]Institute of Chemical Sciences and Centre for Advanced Energy Storage and Recovery, School of Engineering and Physical Sciences, Heriot-Watt University, Edinburgh, EH14 4AS, United Kingdom

[d]CELLS-ALBA Synchrotron, Carrer de la Llum 2-26, 08290, Cerdanyola del Vallès, Barcelona, Spain

[e]Department of Energy Conversion and Storage, Technical University of Denmark, Fysikvej, 2800 Kgs. Lyngby, Denmark

*Corresponding author. Tel.: +92 42 3560 8131; Email address: fsher@lums.edu.pk

*Co-corresponding author. Tel.: +92 33 47497978; Email address: uzma.sps@pu.edu.pk

Abstract

A new series of $Ba_{2-x}Bi_xCoRuO_6$ ($0.0 \leq x \leq 0.6$) hexagonal double perovskite oxides have been synthesized by the solid-state reaction method by substituting Bi with Ba. The polycrystalline materials are structurally characterized at the laboratory, synchrotron X-ray and neutron powder diffraction. The lattice parameters are found to increase with increasing the Bi doping despite the smaller ionic radius of Bi^{3+} compared to Ba^{2+}. The expansion is attributed to the reduction of Co/Ru-site cations. Scanning electron microscopy (SEM) further shows that the grain size increases with Bi content. All $Ba_{2-x}Bi_xCoRuO_6$ ($0.0 \leq x \leq 0.6$) samples exhibit p-type behavior, and the electrical resistivity (ρ) is consistent with small polaron hopping model. The Seebeck coefficient (S) and thermal conductivity (κ) are improved significantly with Bi doping. High values of the power factor ($PF \sim 6.64 \times 10^{-4}$ W/m·K^2) and the figure-of-merit ($zT \sim 0.23$) are obtained at 618 K for $x = 0.6$ sample. These results show that Bi doping is an effective approach for enhancing the thermoelectric properties of hexagonal $Ba_{2-x}Bi_xCoRuO_6$ perovskite oxides.

Keywords: Thermoelectric, Hexagonal perovskite, Bi doping, Seebeck coefficient, Power Factor and Figure-of-merit.

1. Introduction

Climate change, worsening pollution levels and the demands of burgeoning population are the key concerns linked with the present worldwide energy crisis. Effective approaches for recycling of waste heat can play an important role in the sustainable future energy technologies. Conservative estimates suggest that about 40–60% of the total energy that we consume each year is lost to the environment as waste heat.[1] Thermoelectric (TE) power generation offers an attractive way for direct conversion of heat into electric power and is considered an important component of a sustainable future energy mix.[2] Practical TE modules use *p*- and *n*-type semiconductors coupled together electrically in series and thermally in prallel.[3] The performance of thermoelectric materials is estimated by the dimensionless figure-of-merit, zT:[4]

$$zT = \frac{S^2}{\rho\kappa}T = \frac{PF}{\kappa}T \tag{1}$$

Here, S (V/K) is the Seebeck coefficient, ρ ($\Omega\cdot m$) is the electrical resistivity, κ [$\kappa_{\mathrm{el}}+\kappa_{\mathrm{lattice}}$] ($W/m\cdot K$) is the thermal conductivity (sum of the electronic and lattice thermal conductivities), PF ($W/m\cdot K^2$) is the power factor and T (K) is the absolute temperature.

A small value of electrical resistivity or a high value of electrical conductivity, σ, is essential for a low internal resistance. The thermal conductivity of the TE material must be low for maintaining a temperature difference across two ends of the device. A trade-off of these properties for achieving $zT \geq 1$ is necessary for practical applications.[5] In addition, raw material availability, low cost, low toxicity, and high thermal and chemical stabilities are highly desirable characteristics for good thermoelectric materials.[6] The electrical and thermal transport properties of TE materials are strongly correlated with their cryastal structures and chemical compositions. The Seebeck coefficient and thus power factor can be enhanced using various methods such as element doping, energy barrier filtering, additional carrier pocket, resonant states and band engineering or band modifications.[7-9] The improvement of Seebeck coefficient via density-of-states (DOS) modification is a promising way and element doping can be used to fine tune the DOS and obtain the desired band structure.[9] The thermoelectric materials with high Seebeck coefficient generate more thermovoltage per temperature difference ($S = dV/dT$) and thus give better performance at the operating temperature of the device.[10]

The most common thermoelectric materials are alloys of chalcogenides such as Bi_2Te_3, PbTe, $Bi_2Te_{3-x}Se_x$, $Bi_xSb_{2-x}Te_3$ and are based on either bismuth telluride or lead telluride.[1] These materials are relatively scarce (and therefore expensive), toxic and unstable at high temperatures. Transition metal oxides were initially ignored in the search for potential thermoelectric materials until the discovery of high PFs in p-type Na_xCoO_2 about two decades ago.[11] Since then many other metal oxides have been explored and reported as promising thermoelectric materials. For example, ZnO,[12,13] $SrTiO_3$,[14,15] $CaMnO_3$,[16,17] $Ca_3Co_4O_9$[18,19] and $Bi_2Sr_2Co_2O_x$[20] have all shown good TE properties. Yet, the performance of most oxide materials is still lower than the non-oxide traditional thermoelectric materials, and the effort is still ongoing for search of efficient novel TE metal oxides.

Double perovskite (DP) oxides having the general formulae A_2BRuO_6, where A is the alkaline-earth or rare earth metal and B is the transition metal, show very interesting magnetic and electronic properties.[21,22] These oxides crystallize in 6 layered hexagonal crystal structure when larger size ions like Ba^{2+} are present at the A-site of the perovskite, as it was firstly reported for one of the polymorphs of $BaTiO_3$.[23] The Goldschimdt tolerance factor ($t = (r_A + r_O)/\sqrt{2}(r_B + r_O)$) for hexagonal perovskite oxides is always greater than 1.0, e.g., for Ba_2CoRuO_6 compund t = 1.06. Here, r_A, r_B and r_O are the Shannon radii of the participating A-site, B-site and oxygen ions. Few examples of interesting Ba containing 6H-hexagonal perovskite oxides are Ba_2CoRuO_6,[21] Ba_2CrMoO_6,[24] Ba_2FeSbO_6 & $Ba_2CoSbO_{6-\delta}$,[25] Ba_2CoTeO_6[26] and Ba_2ScRuO_6.[27] Fig. 1 displays the crystal structure of $Ba_{1.8}Bi_{0.2}CoRuO_6$ compound with 6 layered hexagonal (6H) perovskite type structure, which is similar to that established by H. Bader and S. S. Kemmler.[28]

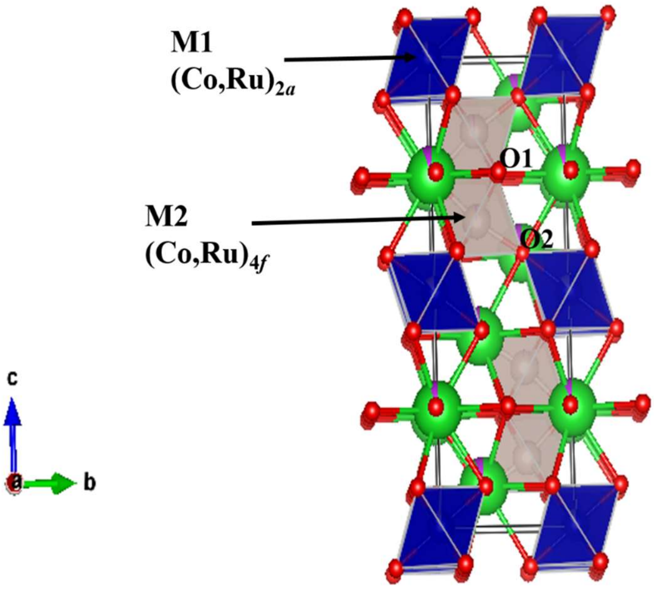

Figure 1 Representation of the 6H-perovskite structure for $Ba_{1.8}Bi_{0.2}CoRuO_6$ sample defined in the *P6₃/mmc* space group symmetry. Ba, Bi, and O atoms are denoted by green, purple and red spheres, respectively, and M2-$(Co,Ru)_{4f}O_6$ octahedra (grey) make dimer units and sharing a common face through oxygen (O1) atoms; these units are linked through M1-$(Co,Ru)_{2a}O_6$ octahedra (blue) sharing corners through oxygen (O2) atoms along the *c*-axis.

In view of the interesting physical properties of hexagonal perovskite oxides, we measured and found that Ba_2CoRuO_6 oxide has low electrical resistivity and high Seebeck coefficient values at room temperature. As reported elsewhere, Bi substitution in $CaMnO_3$ and $Ca_3Co_4O_9$ oxide systems significantly decreases ρ and κ.[29-31] Considering the potentially good thermoelectric properties of

Ba_2CoRuO_6 at room temperature and to understand the structure-property relation, we have substituted Ba with Bi and prepared a series of new $Ba_{2-x}Bi_xCoRuO_6$ ($0.0 \leq x \leq 0.6$) *p*-type semiconductors. Our results show that all synthesized materials, especially $x = 0.6$ composition, present promising thermoelectric properties.

2. Experimental

Polycrystalline $Ba_{2-x}Bi_xCoRuO_6$ ($0.0 \leq x \leq 0.6$) samples were synthesized using solid-state reactions. The powder form of $BaCO_3$, (Sigma-Aldrich ≥ 99 % purity), Bi_2O_3 (Sigma Aldrich ≥ 99.9 % purity), Co_3O_4 (Sigma Aldrich ≥ 99.8 % purity) and RuO_2 (Sigma Aldrich ≥ 99.9 % purity) were mixed for 30 min in stoichiometric ratio in a mortar and pestle. Subsequently, cold-pressed pellets of the powder mixtures were fired at 900 °C in air for a period of 8 h with a heating rate of 10 °C/min. After cooling to room temperature, the mixtures were reground, repelletized and sintered twice at 1150 °C for 8 h in air, when phase pure compounds were obtained.

In order to perform phase analysis and to check the purity of the synthesized samples, laboratory X-ray powder diffraction (XRD) data were recorded on a Bruker D8 Advance X-ray diffractometer (CuK_α radiation, $\lambda = 1.5406$ Å) by step scanning over the angular range of $15 \leq 2\theta \leq 100°$. High angular resolution synchrotron X-ray powder diffraction (SXRD) data were collected at the BL04-MSPD beamline of the ALBA Synchrotron Light Facility (Barcelona, Spain).[32] For collection of synchrotron data (with $\lambda = 0.4426$ Å), the powder samples were sealed in a 0.3 mm diameter capillary to limit X-ray absorption. Data were collected using the MAD26 detector setup, which consists of 13 Si analyzer crystals (Silicon 111 reflection) and scintillator/PMT detectors separated by angular offsets of ~ 1.5°.[33] Data for each sample were recorded between $2 \leq 2\theta \leq 49°$ with a collection time of 48 minutes. Neutron powder diffraction (NPD) data were collected on the high resolution [super-D2B] powder diffractometer at the Institut Laue-Langevin (ILL, Grenoble, France). The neutron wavelength was λ =1.594 Å and it was calibrated using a $Na_2Ca_3Al_2F_{14}$ reference sample. The powder contained in a thin-walled V can of 5 mm diameter, and the diffraction patterns were recorded between $2 \leq 2\theta \leq 160^o$ at room temperature. Rietveld analysis was carried out using general structure analysis system (GSAS) software[34] and the crystal structure was drawn with the visualization for electronic and structural analysis (VESTA) software.[35] The instrument parameters (Thompson-Cox-Hasting and asymmetry profile coefficients) for SXRD data refinements were obtained from the refinement of $Na_2Ca_3Al_2F_{14}$ and a NIST Si standard was used to determine the SXRD wavelength.[36] The particle sizes and morphological features of all the samples were examined by scanning electron microscopic (SEM) analysis.

High temperature Seebeck coefficient and electrical resistivity data were collected on a Linseis LSR-3 instrument in a He atmosphere between 300−673 K. This used rectangular bars of approximate $3 \times 4 \times 16$ mm^3 dimensions, which were cut from the sintered pellets. The thermal conductivity was calculated from the equation: $k = C_p \cdot d \cdot \alpha$, where '$C_p$' is the heat capacity, 'd' is the bulk density and 'α' is the thermal diffusivity. The 'α' was measured on a laser flash instrument [Netszch-LFA-457] under vacuum. The Dulong−Petit value was used for C_p. The densities of all the bulk samples were estimated using the Archimedes principle and fall in between 88−95 % (Table 4).

3. Results and discussion

3.1. Room temperature crystal structure and morphological study

The crystal structures of hexagonal $Ba_{2-x}Bi_xCoRuO_6$ $(0.0 \leq x \leq 0.6)$ perovskite oxides were studied using XRD, SXRD and NPD at room temperature. The XRD patterns shown in Fig. 2(a) indicate that all samples are single phase, without any noticeable amount of secondary phase, demonstrating that we can obtain single phase perovskites using the conventional solid-state synthesis process. The XRD peaks can all be indexed on the previously reported hexagonal 6H crystal structure for Ba_2CoRuO_6.[21] The XRD (104) zoomed peaks of the studied samples are presented in Fig. 2(b), which demonstrate the effect of Bi doping on the crystal structure of Ba_2CoRuO_6. The XRD reflections shift to lower 2θ values with increasing Bi content. The Rietveld refinement was carried out on XRD data using the hexagonal 6H crystal structure with $P6_3/mmc$ (No. 194) space group for all samples. The refined crystallographic parameters and reliability factors are listed in Table 1 and the representative bond lengths and bond angles are summarized in Table 2. The refinement quality parameters like Weighted profile residual (R_{wp}), Profile residual (R_p) and Goodness of fit (χ^2) (Table 1) are reasonably low and confirm the reliability of the fitted structures. Fig. 3 displays the variation of lattice parameters and unit cell volumes with increasing Bi content. These values show a sudden increase from $x = 0$ to $x = 0.1$ and then increase gradually with increasing Bi content. The expansion of the unit cell goes against the expected trend based on the A-cation radius since Bi^{3+} (1.17 Å, 8-fold coordination) is smaller than Ba^{2+} (1.42 Å). This suggests that it is related to the reduction of the B-site cations, expected oxidation states of Co^{3+} and Ru^{5+} in Ba_2CoRuO_6 that must occur upon Bi^{3+} substitution, assuming a constant oxygen content. Bond valence sum calculations based on the NPD data (below) recommend oxidation states of Co^{3+} and Ru^{4+} in $x = 0.2$ and $x = 0.3$ samples, proposing that the reduction of Ru causes the lattice expansion.

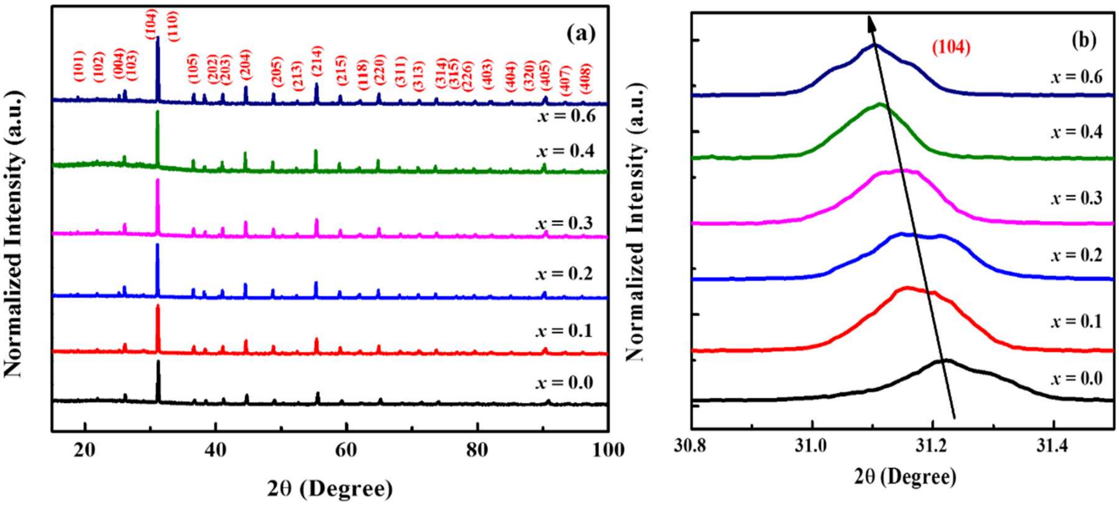

Figure 2 Room temperature X-ray diffraction (XRD) patterns of (a) $Ba_{2-x}Bi_xCoRuO_6$ ($0.0 \le x \le 0.6$) samples, and (b) (104) peak details.

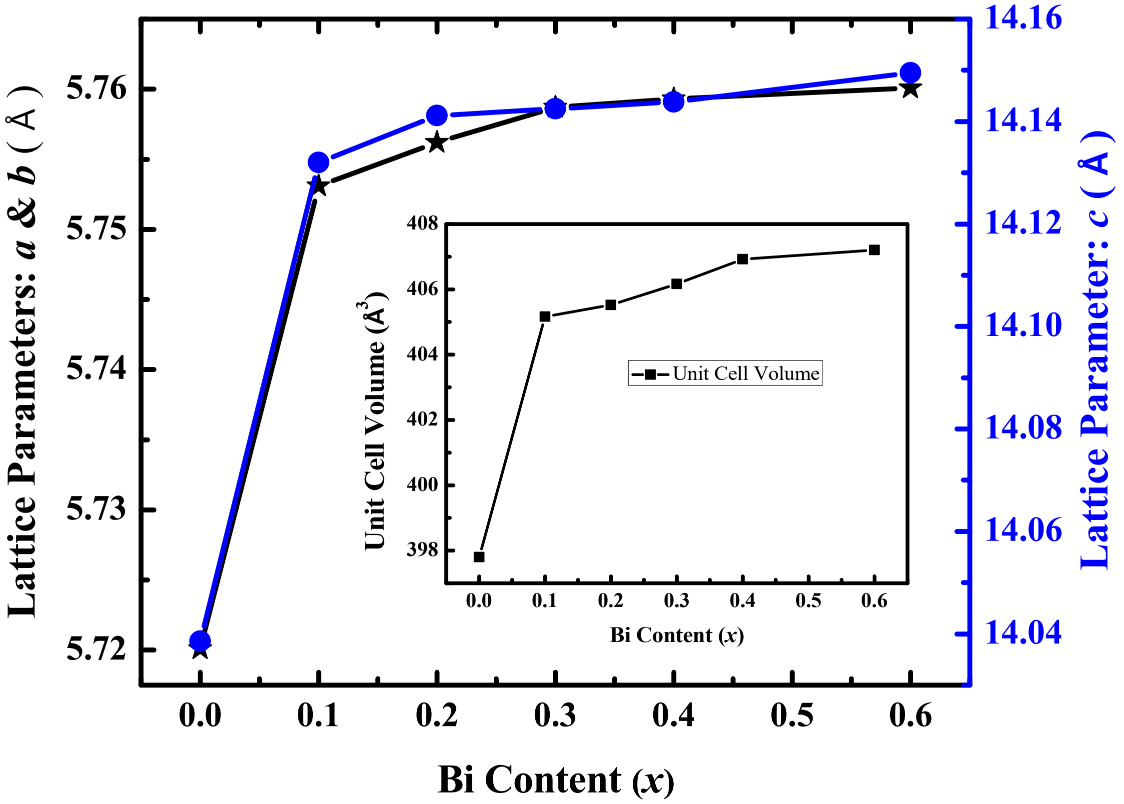

Figure 3 Variation in the lattice parameters, *a*, *b* & *c* and unit cell volumes (*V*) (inset) as a function of Bi doping contents for $Ba_{2-x}Bi_xCoRuO_6$ ($0.0 \leq x \leq 0.6$) samples.

Table 1 Refined structural parameters for $Ba_{2-x}Bi_xCoRuO_6$ ($0 \leq x \leq 0.6$) samples determind from s
diffraction (SXRD), neutron powder diffraction (NPD) and X-ray diffraction (XRD) data at ro

$Ba_{2-x}Bi_xCoRuO_6$	$x = 0.0$	$x = 0.1$	$x = 0.2$	$x = 0.2$	$x = 0.3$	$x = 0.3$
Space group	*P6₃/mmc*	*P6₃/mmc*	*P6₃/mmc*	*P6₃/mmc*	*P6₃/mmc*	*P6₃/mmc*
Structure	*Hexagonal*	*Hexagonal*	*Hexagonal*	*Hexagonal*	*Hexagonal*	*Hexagonal*
Lattice Parameters						
***a* (Å)**	5.7200(4)	5.7537(6)	5.7565(3)	5.7529(4)	5.7586(3)	5.7587(5)
***b* (Å)**	5.7200(4)	5.7537(6)	5.7565(3)	5.7529(7)	5.7586(3)	5.7587(4)
***c* (Å)**	14.0393(2)	14.1322(2)	14.1414(3)	14.1303(2)	14.1427(6)	14.1428(7)
Volume $(Å)^3$	397.805(8)	405.173(2)	405.46(2)	405.008(5)	406.169(5)	406.175(4)
Atomic Positions						
A1 (Ba/Bi)						
Site 2(*b*)						
x	0.0	0.0	0.0	0.0	0.0	0.0
y	0.0	0.0	0.0	0.0	0.0	0.0
z	¼	¼	¼	¼	¼	¼
U_{iso}*100/$(Å)^2$	0.83(2)	0.94(3)	0.54(2)	0.773(17)	0.92(3)	0.932(19)
Occ[Ba(1)]	1.00	0.90(2)	0.910(5)	0.958(4)	0.917(10)	0.877(7)
Occ[Bi(1)]	0.0	0.096(5)	0.090(5)	0.042(4)	0.083(10)	0.123(7)
A2 (Ba/Bi)						
Site 4(*f*)						
x	1/3	1/3	1/3	1/3	1/3	1/3
y	2/3	2/3	2/3	2/3	2/3	2/3
z	0.9101(6)	0.9111(2)	0.9104(2)	0.9105(2)	0.9102(5)	0.9102(3)
U_{iso}*100/$(Å)^2$	0.96(2)	1.00(2)	0.88(1)	0.963(11)	1.02(1)	1.037(17)
Occ[Ba(2)]	1.00	0.904	0.877(4)	0.928(3)	0.917(9)	0.879(6)
Occ[Bi(2)]	0.0	0.087(8)	0.123(4)	0.071(3)	0.083(9)	0.121(6)
M1 (Co/Ru/Bi)						
Site 4(*a*)						
x	1/3	1/3	1/3	1/3	1/3	1/3
y	2/3	2/3	2/3	2/3	2/3	2/3
z	0.1549(7)	0.1542(2)	0.1543(2)	0.1544(2)	0.1546(2)	0.1546(3)
U_{iso}*100/$(Å)^2$	0.45(3)	0.54(3)	0.28(2)	0.358(12)	0.58(2)	0.560(19)

Occ[Co]	0.276	0.228	0.21(0)	0.121(2)	0.216(1)	0.143(8)	-	-
Occ[Ru]	0.724	0.684	0.637(2)	0.828(6)	0.648(4)	0.725(3)	-	-
Occ[Bi]	0.0	0.087	0.142	0.051(3)	037(5)	0.132(2)	-	-
M2 (Co/Ru)								
Site 4(*f*)								
x	0.0	0.0	0.0	0.0	0.0	0.0	0.0	0.0
y	0.0	0.0	0.0	0.0	0.0	0.0	0.0	0.0
z	0.0	0.0	0.0	0.0	0.0	0.0	0.0	0.0
U_{iso}*100/(Å)^2	0.33(5)	0.74(6)	1.12(5)	0.619(6)	0.82(6)	0.773(2)	-	-
Occ[Co(2)]	1.00	0.77(2)	0.822(9)	0.900(5)	0.812	0.804(9)	-	-
Occ[Ru(2)]	0.0	0.23(2)	0.178(9)	0.100(5)	0.188	0.196(9)	-	-
O(1)								
Site 6(*h*)								
x	0.4855(6)	0.4851(6)	0.4863(6)	0.4847(2)	0.4859(6)	0.4845(3)	0.4861(21)	0.4896(12)
y	−0.0289(12)	−0.0298(11)	−0.0273(13)	−0.0305(3)	−0.0281(12)	−0.0309(5)	−0.0279(4)	−0.0208(6)
z	¼	¼	¼	¼	¼	¼	¼	¼
U_{iso}*100/(Å)^2	1.00(6)	0.59(8)	0.37(6)	0.671(5)	0.683(7)	0.593(5)	-	-
Occ[O(1)]	1.00	1.00	1.00	1.00	1.00	1.00	-	-
O(2)								
Site 12(*k*)								
x	0.1669(5)	0.1697(5)	0.1654(5)	0.1699(2)	0.1678(5)	0.1709(2)	0.1672(15)	0.1680(23)
y	0.3338(10)	0.3395(10)	0.3309(11)	0.3399(4)	0.3355(10)	0.3417(5)	0.3344(3)	0.3360(5)
z	0.4179(3)	0.4161(3)	0.4160(3)	0.4166(1)	0.4160(3)	0.4166(3)	0.4145(7)	0.4142(10)
U_{iso}*100/(Å)^2	1.00(6)	0.59(8)	0.37(6)	0.800(16)	0.683(7)	0.593(2)	-	-
Occ[O(2)]	1.00	1.00	1.00	1.00	1.00	1.00	-	-
Reliability Factors								
R_{wp} (%)	5.6	5.2	6.5	3.60	6.2	5.04	6.5	5.8
R_p (%)	4.4	4.1	4.8	2.74	4.8	3.88	4.9	4.6
χ^2 (%)	1.26	1.24	1.72	2.41	1.72	2.56	1.85	1.26
Crystallite Size								
D (*nm*)	30.0	60.0	100.0	-	130.0	-	160.0	200.0

The structure was refined by using a SXRD (x = 0.0, 0.1, 0.2 & 0.3), combined SXRD and NPD (x = 0.2 & 0.3) and laboratory XRD (x = 0.4 & 0.6) data set.

Table 2 Selected bond lengths (Å) and bond angles (°) for $Ba_{2-x}Bi_xCoRuO_6$ ($0 \leq x \leq 0.6$) samples from Rietved anlasysis of XRD data.

Composition $Ba_{2-x}Bi_xCoRuO_6$	**x = 0.0**	**x = 0.1**	**x = 0.2**	**x = 0.3**	**x = 0.4**	**x = 0.6**
Bond Lengths (Å)						
Co/Ru$_1$–O$_1$ × 3	2.026(16)	2.123(14)	2.096(15)	2.146(15)	2.127(16)	2.295(31)
Co/Ru$_1$–O$_2$ × 3	1.904(14)	1.944(14)	1.941(16)	1.931(14)	1.926(14)	1.940(29)
Co$_2$–O$_2$ × 6	2.055(14)	2.027(13)	2.040(15)	2.041(14)	2.051(14)	2.045(14)
Co/Ru$_1$–Co$_2$ × 6	3.956(2)	3.965(2)	3.976(2)	3.969(2)	3.971(2)	3.974(2)
Ba$_1$/Bi$_1$–O$_1$ × 6	2.863(2)	2.86961)	2.873(2)	2.874(3)	2.876(5)	2.885(4)
Ba$_1$/Bi$_1$–O$_2$ × 6	2.873(15)	2.842(13)	2.843(15)	2.877(14)	2.846(14)	2.879(0)
Ba$_2$/Bi$_2$–O$_1$ × 3	2.868(15)	2.809(12)	2.836(13)	2.840(12)	2.833(13)	2.884(3)
Ba$_2$/Bi$_2$–O$_2$ × 3	2.862(3)	2.870(5)	2.873(2)	2.875(2)	2.876(2)	2.878(5)
Ba$_2$/Bi$_2$–O$_2$* × 3	2.931(16)	2.984(14)	2.980(16)	2.895(3)	2.981(15)	3.040(3)
Bond Angles (deg)						
O$_2$–Co$_2$–O$_2$	89.8(6)	88.6(5)	88.7(6)	89.8(5)	88.5(6)	87.2(11)
Co$_2$–O$_2$–Co/Ru$_1$	176.5(9)	175.5(8)	174.4(9)	174.0(8)	173.6(8)	171.8(16)

Fig. 4 displays the Rietveld fits to the SXRD data for the x = 0.0, 0.1, 0.2 and 0.3 samples. The refined crystallographic parameters including atomic positions, thermal parameters, fractional occupancies, and R-factors are summarized in Table 1. The Rietveld analysis unexpectly suggested that Bi replaces a fraction of the Co/Ru ions along with substituting on the intended Ba position. In order to further assess the possibility of Bi substitution on the *B*-site, we used a combined Rietveld refinement of SXRD and NPD data for $Ba_{2-x}Bi_xCoRuO_6$ (x = 0.2 and 0.3, See Fig. 5). A drawing of the crystal structure is shown in Fig. 1, which represents the existance of (M2: Co,Ru)O_6 dimer units of octahedra (Co and Ru at 4*f*-sites) sharing a face positions through the O1 atoms. The dimers are linked along the *c*-axis direction through a single (M1: Co,Ru)O_6 octahedra (at 2*a*-sites) sharing corners through the O2 atoms.The selected interatomic bond distances and bond angles are listed in Table 2. Ferreira, *et al.*,[37] have reported that B−O−B′ bond angles in the ideal cubic double perovskite structure are 180°, and they observed that this value reduces for the

M−O−Ir bonds in the Ln_2MIrO_6 (Ln = Pr, Nd, Sm−Gd: M = Ni, Mg) materials with decreasing size of the lanthanide ion from La−Gd due to structural distortion and decreasing A-site cation size relative to the B-sites. Table 2 also shows that Co−O−Ru bond angles are decreasing with increasing Bi substitution. As anticipated, decreasing Co−O−Ru bond angles result from the increased structural distortion in our system. The estimated bond valence sum (BVS) of 4.02 (M1 & M2-sites) and 4.00 (M1 & M2-sites) are representative of Ru^{4+} and 3.12 (M1 & M2-sites) and 3.10 (M1 & M2-sites), are indicative of Co^{3+} for $x = 0.2$ and $x = 0.3$ samples, respectively (See Table 3). Refinement of site-occupancies for oxygen atoms did not provide evidence of any major differences from full occupancy values, therefore, these numbers were kept fixed during the refinement. The refined composition is $Ba_{1.87}Bi_{0.19}Co_{0.76}Ru_{1.17}O_6$ for $x = 0.2$, hence showing no evidence for Bi substitution on the Co/Ru sites.

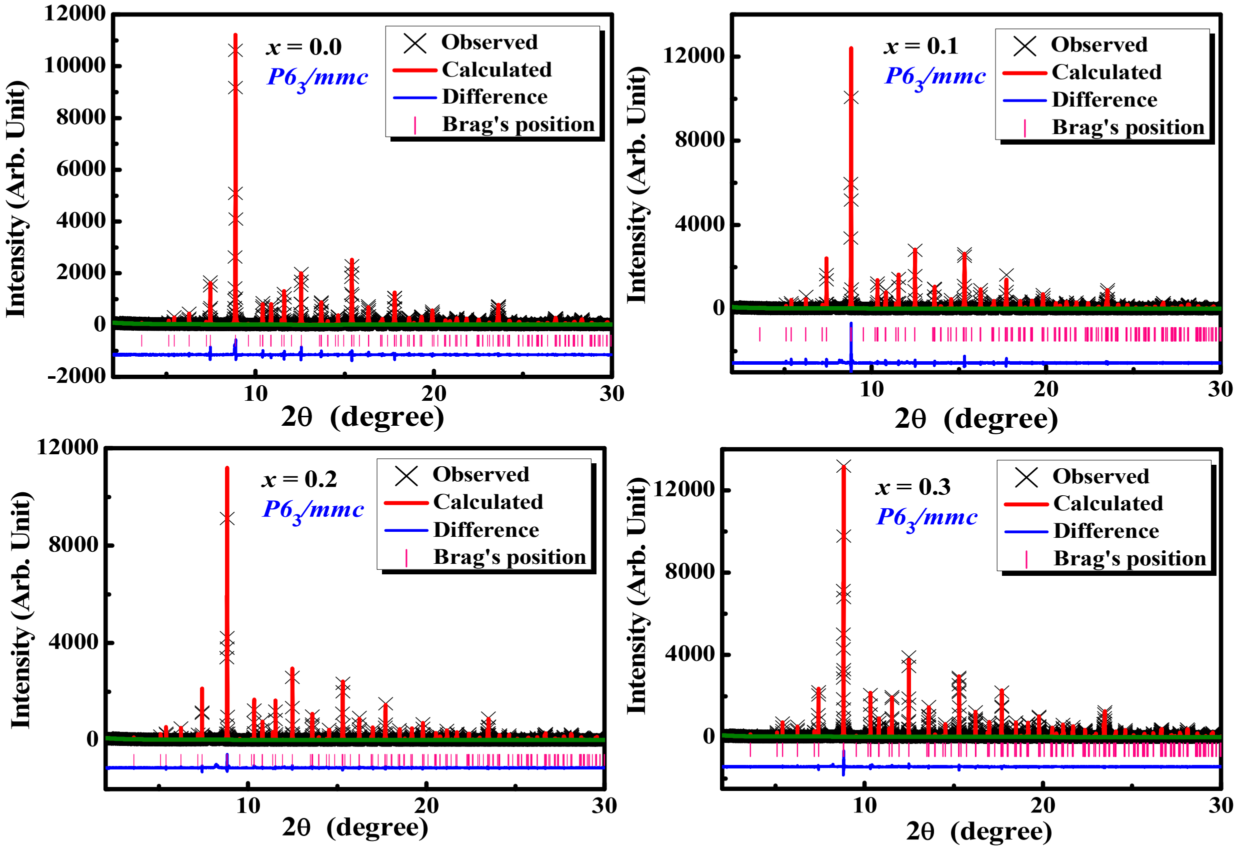

Figure 4 Rietveld analysis of powder synchrotron X-ray diffraction data obtained with MAD detector for the $Ba_{2-x}Bi_xCoRuO_6$ ($0 \leq x \leq 0.3$) samples.

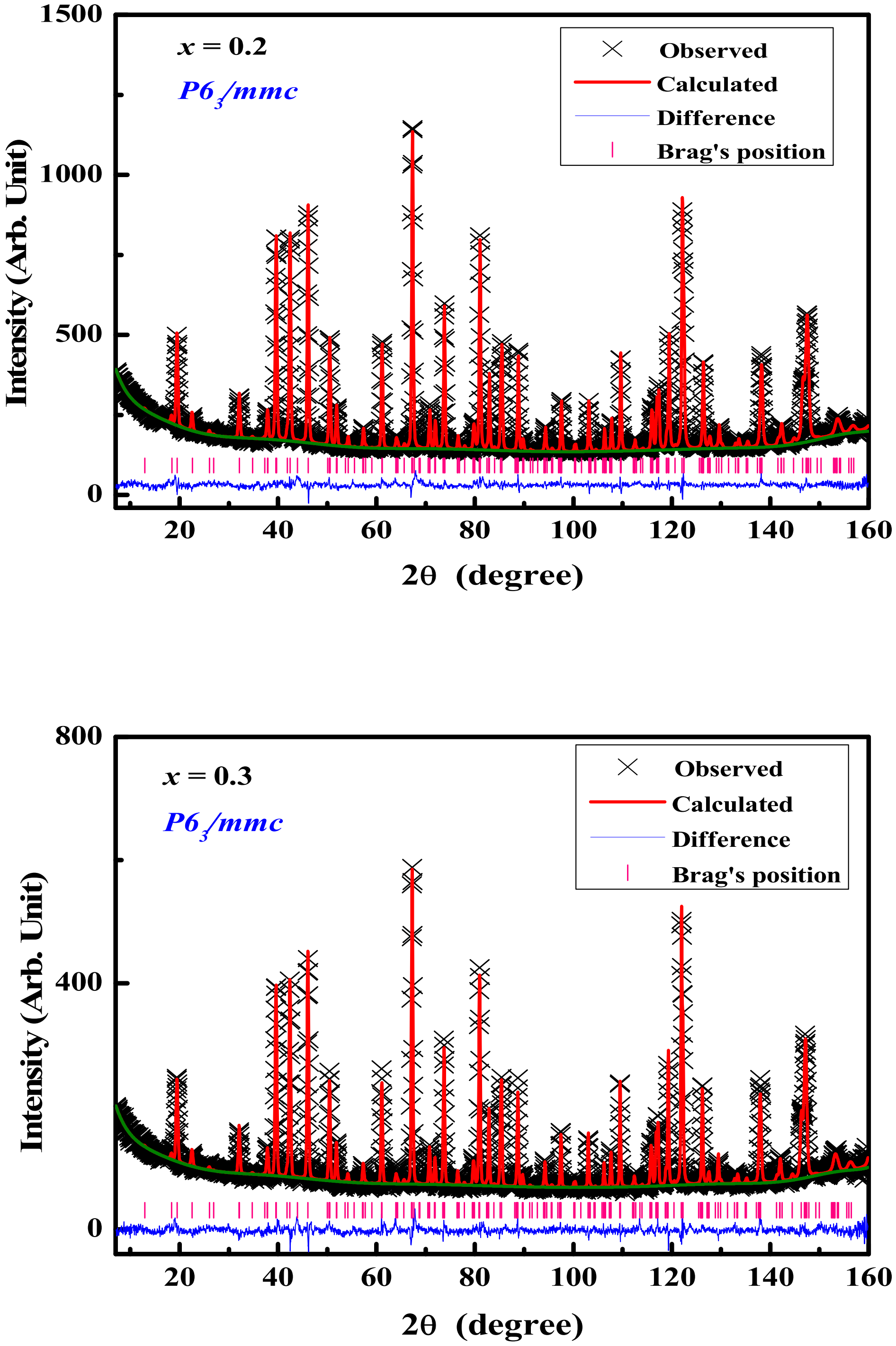

Figure 5 Rietveld refinement profiles of room temperature NPD patterns for $Ba_{2-x}Bi_xCoRuO_6$ ($x = 0.2$ and 0.3).

Table 3 Bond Valence Sum (BVS) calculation from NPD data.

Composition $Ba_{2-x}Bi_xCoRuO_6$	**$x = 0.2$**	**$x = 0.3$**
$Co_1{-}O_1 \times 2$	2.0243(12)	2.0335(18)
$Co_1{-}O_2 \times 2$	1.9129(17)	1.9148(14)
$Co_1{-}O_1$	2.0247(12)	2.0339(18)
$Co_1{-}O_2$	1.9125(17)	1.9144(17)
BVS	3.12	3.10
$Ru_1{-}O_1 \times 2$	2.0243(12)	2.0335(18)
$Ru_1{-}O_2 \times 2$	1.9129(17)	1.9148(13)
$Ru_1{-}O_1$	2.0247(12)	2.0339(18)
$Ru_1{-}O_2$	1.9125(17)	1.9144(13)
BVS	4.02	4.00

The crystallite size is extracted for $Ba_{2-x}Bi_xCoRuO_6$ ($0.0 \leq x \leq 0.6$) samples from Rietveld analysis of XRD data and presented in Table 1. It is observed that crystallite size increases from 30.0 *nm* ($x = 0$) to 200.0 *nm* and this is consistent with the observed higher bulk density of Bi-doped samples. Fig. 6 displays SEM images of the $Ba_{2-x}Bi_xCoRuO_6$ samples, which were sintered at 1150 °C. These data confirm the increase in crystallite/grain size inferred from the diffraction data and can be explained by the presence of Bi. The solid-state chemical reactions consist of four main steps of diffusion, reaction, nucleation and crystal growth. When the diffusion rate is faster and the nucleus's growth rate is greater than the nucleation rate at the given reaction conditions, larger crystals are formed. The low melting point of Bi_2O_3 (817 °C) compared to $BaCO_3$ (1360 °C) suggests that the diffusion of Bi^{3+} cations will be faster than Ba^{2+} and consequently the crystallite/grain size will be larger in the Bi doped samples for the given sintering time and temperature.[38-40] Moreover, the increase of crystallite size (D) with doping is also correlated with increase of lattice distortion in the materials.[41]

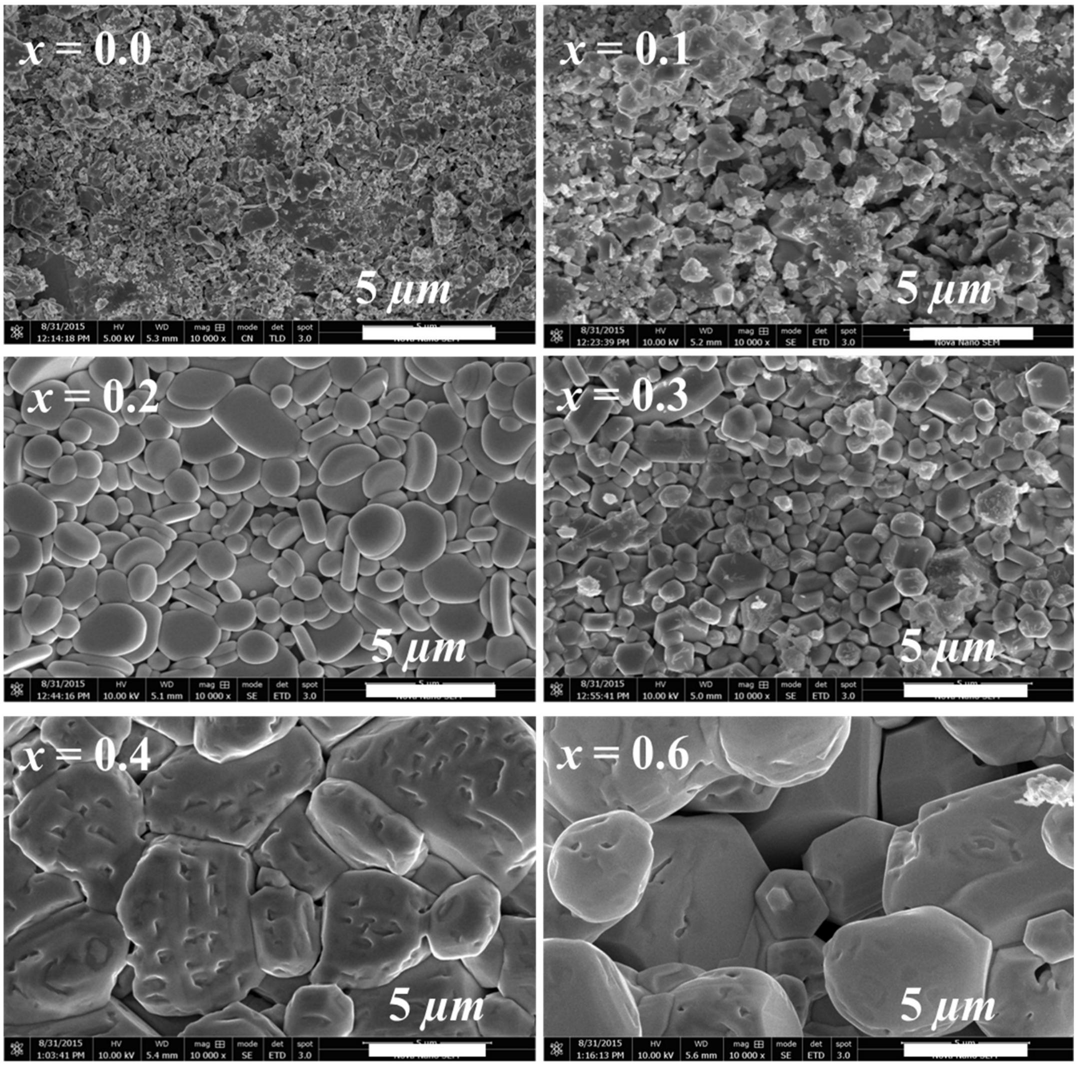

Figure 6 Scanning electron microscope (SEM) images for $Ba_{2-x}Bi_xCoRuO_6$ ($0.0 \leq x \leq 0.6$) samples.

3.2. Thermoelectric properties

Fig. 7(a) shows the temperature dependent electrical resistivity (ρ) for the $Ba_{2-x}Bi_xCoRuO_6$ ($0.0 \leq x \leq 0.6$) samples. The electrical resistivity decreases with increasing temperature for all samples, confirming a semiconducting-like ($d\rho/dT < 0$) behavior. It is observed that ρ increases with Bi doping in $Ba_{2-x}Bi_xCoRuO_6$ perovskite oxides. This increase in ρ is consistent with the *n*-type doping resulting from replacement of Ba^{2+} by Bi^{3+} cations, which would decrease the *p*-type carrier concentration. Similar trend has been reported previously in the Bi and Eu-doped $Ca_3Co_4O_9$ materials.[42,43] The valence electronic configuration of Bi is $6s^2 6p^3$, therefore, $6s^2$ lone pair of electrons on Bi^{3+} are known to induce structural distortion, which was explaind initialy in $BiMnO_3$ materials.[44] Moreover, the increase in ρ in our Bi doped samples can also be caused by the increasing structural distortion and a decreasing carrier mobility.

Electronic conduction in perovskite oxides cannot usually be entirely described by a band model.[45] Instead, charge carriers are typically localized at the defect sites associated with activation energy (E_a) barrier for the charge carriers to become delocalized. A small polaron hopping model seems to be the best choice to explain conduction mechanism in these materials.[46] Hopping conduction takes place when ions of different valence states like Co^{3+} and Ru^{4+} occupy same crystallographic sites and then charge carriers can be transported through the solid material with associated field polarization, which is known as the quasi particle (polaron). A small polaron hopping model can be represented by the following equation.[47]

$$\rho(T) = \rho_0 T \exp\left(\frac{E_a}{k_B T}\right) \tag{2}$$

where, ρ_0 is the residual resistivity, k_B is the Boltzmann constant and E_a is the activation energy of electrical conductivity for hopping conduction. Fig. 7(b) shows the linear fiting of ln(ρ/T) vs. $1/T$ from room temperature to 618 K and the "small-polaron hopping model" describes the data reasonably well. The slopes of straight lines (E_a/k_B) were used to calculate the activation energies for all $Ba_{2-x}Bi_xCoRuO_6$ ($0.0 \le x \le 0.6$) samples as listed in Table 4. It has been observed that activation energies of Bi doped samples are larger than the undoped Ba_2CoRuO_6 system, indicating that Bi doping increases the energy barrier for hopping carriers conduction in these materials. Similar trend in the activation energies has also been reported for other Bi doped perovskite oxides as well.[48] The values of E_a (Table 4) are affected by the Bi^{3+} doping and the activation energies for Bi-doped samples are higher than the undoped Ba_2CoRuO_6 material. This increase in E_a can be explained by considering the Co^{3+}-$Ru^{5+/4+}$ d^6-$d^{3/4}$ (low spin) paths $t_{2g}{}^6$ - $t_{2g}{}^{3/4}$, so there is a change from 2 → 1 holes in the t_{2g} band with Bi substitution, which is consistent with the higher activation energies for doped samples.

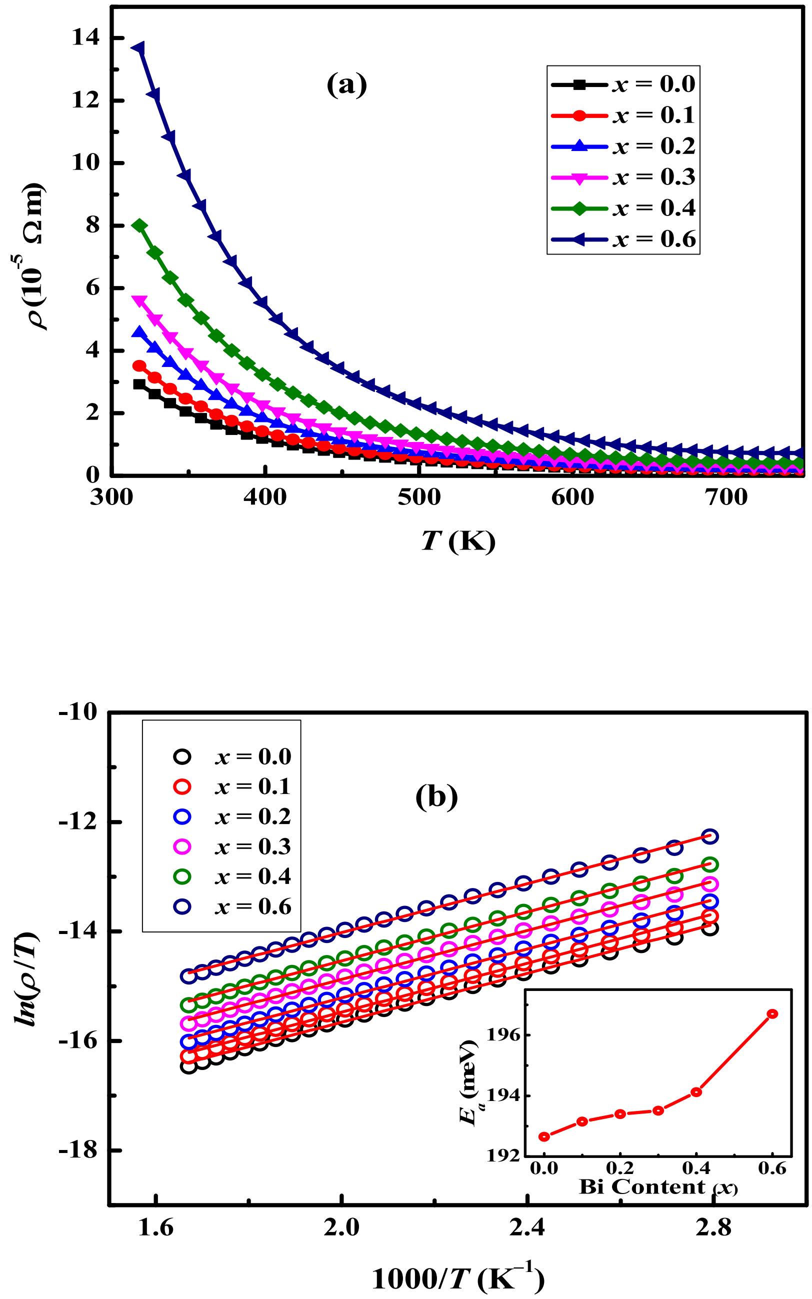

Figure 7 Temperature dependent electrical resistivity for Ba$_{2-x}$Bi$_x$CoRuO$_6$ ($0.0 \le x \le 0.6$) samples (a); the small-polaron hopping model fitting for electrical resistivity data for Ba$_{2-x}$Bi$_x$CoRuO$_6$ ($0.0 \le x \le 0.6$) samples. The solid lines and empty symbols represent fitting and experimental data, respectively. The activation energy (E_a) for Ba$_{2-x}$Bi$_x$CoRuO$_6$ ($0.0 \le x \le 0.6$) compounds, Inset (b).

Table 4 Bulk density, activation energies, E_a and Es, and important thermoelectric parameters of samples.

Composition $Ba_{2-x}Bi_xCoRuO_6$	***x* = 0.0**	***x* = 0.1**	***x* = 0.2**	***x* = 0.3**	***x* = 0.4**	***x* = 0.6**
Density (g/cm^3)	5.86	6.31	6.43	6.47	6.50	6.67
Theoretical Density (g/cm^3)	6.639	6.663	6.864	6.886	6.890	7.042
Relative Density (%)	88.26	94.70	93.67	93.95	94.33	94.71
E_a (meV)	192.65	193.15	193.40	193.51	194.12	196.70
Es (meV)	13.97	16.77	20.12	25.15	40.25	77.28
$\rho_{T=318K} \times 10^{-5}$ (Ω m)	2.93	3.51	4.57	5.63	8.01	1.37
$\rho_{T=618K} \times 10^{-5}$ (Ω m)	2.24	2.69	3.49	4.31	6.13	1.05
$S_{T=318K}$ (μV/K)	54.52	65.42	78.51	98.13	157.01	301.47
$S_{T=618K}$ (μV/K)	11.97	14.36	17.23	21.54	34.46	66.17
$PF_{T=318K} \times 10^{-4}$ (W/m·K^2)	1.01	1.21	1.34	1.70	3.08	6.64
$PF_{T=618K} \times 10^{-4}$ (W/m·K^2)	0.64	0.77	0.85	1.08	1.93	4.17
$\kappa_{T=318K}$ (W/m·K)	1.48	1.44	1.70	1.39	1.32	1.20
$\kappa_{T=618K}$ (W/m·K)	1.42	1.31	1.08	1.24	1.19	1.09
$zT_{T=318K}$	0.022	0.027	0.030	0.039	0.073	0.18
$zT_{T=618K}$	0.028	0.036	0.040	0.053	0.10	0.23

The Seebeck coefficients (S) for the $Ba_{2-x}Bi_xCoRuO_6$ ($0.0 \leq x \leq 0.6$) samples as a function of temperature (T) are shown in Fig. 8(a). All S values are positive for these samples, confirming *p*-type conduction behavior. The magnitude of S decreases with increase in temperature for all samples, which is signifying semiconducting like behavior of the materials. It is also noticeable from Fig. 8(a) that the Seebeck coefficient increases with increasing Bi doping. The S values at 318 K and 618 K are listed in Table 4 for all samples. The maximum Seebeck coefficient of ~301 μV/K is obtained for $x = 0.6$ sample at room temperature. This value is significantly higher than the reported S values for Sr_2CoTiO_6[49] (122 μV/K), Sr_2MnMoO_6[50] (200 μV/K), Sr_2FeTiO_6[51] (~ 150

μV/K) and $Ba_xSr_{2-x}FeTiO_6$[51] with x = 0.25 (~ 200 μV/K) samples at room temperature. The compositions with more than x = 0.6 doping contents are not examined for thermoelectric properties because the perovskite structure breaks up after the optimum amount of Bi-doping. There are very few metal oxides which exhibit such a high magnitude of the Seebeck coefficient at room temperature. This observation has prompted us to explore double perovskite oxide based thermoelectric materials further.

Mott-adiabatic small polaron conducting model has been used to calculate the activation energies (E_S) from the Seebeck coefficient data. The relevant equation is given below.[52]

$$S(T)=\frac{k_B}{e}\left(\frac{E_S}{k_BT}\right)+S_\infty \qquad (3)$$

where, e is the electronic charge and k_B is the Boltzmann constant, S_∞ is the Seebeck coefficient at the asymptotically high temperature and calculation of the entropy of magnetic and crystalline materials disorders/defects. The activation energies (E_S) are calculated from the slopes of linear fits of S vs $1/T$ data (Fig. 8(b)). The calculated E_S values for all samples are listed in Table 4. The large difference between the activation energies obtained from the electrical resistivity (E_a) and Seebeck coefficient (E_S) data suggests that typical "band transport" mechanism is not valid for the studied samples, rather the transport mechanism in these samples can be explained by the "small-polaron hopping-model". In this model, the transport of the charge carriers is carried out through temperature dependent mobility effects.[53] Activation energy (E_a) from $\rho(T)$ is the total energy needed for creating and hoppog of carriers, whereas E_S is the energy required for only activating the carriers hopping. Consequently, values of the activation energy (E_a) are always higher than the activation energies (E_S) i.e., $E_a > E_S$ for all samples following the small-polaron hopping-model.

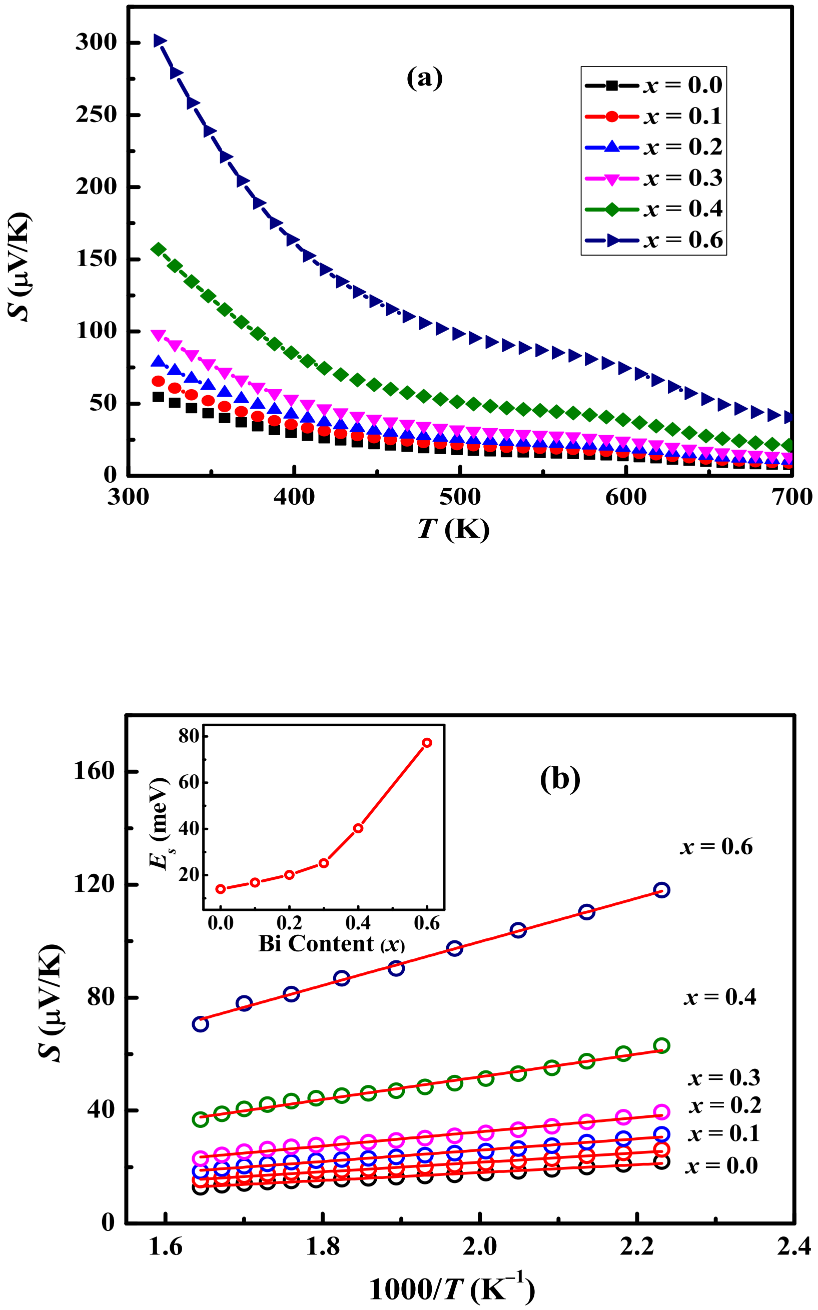

Figure 8 Temperature dependent Seebeck coefficient (S) for the $Ba_{2-x}Bi_xCoRuO_6$ ($0.0 \le x \le 0.6$) samples (a); the S vs. 1/T for $Ba_{2-x}Bi_xCoRuO_6$ ($0.0 \le x \le 0.6$) samples. The solid lines and empty symbols represent fitting and experimental data, respectively. The activation energy (E_s) for $Ba_{2-x}Bi_xCoRuO_6$ ($0.0 \le x \le 0.6$) samples, Inset (b).

Fig. 9(a) shows thermoelectric power factor (*PF*) as a function of temperature for all samples. The values of the *PF* are higher at room temperature for all samples and then decrease with increasing temperature. This trend follows the Seebeck coefficient data, which also decrease with temperature. The *PF* values increase significantly with increasing Bi doping at room temperature and the highest value of $\sim 6.6 \times 10^{-4}$ W/m·K^2 is achieved for $x = 0.6$ sample at 318 K. Though, the effect of Bi doping on the *PF* is small at higher temperatures. The observed power factors are higher than the previously published results for cubic double perovskite oxide materials (See Table 5), which suggests that 6H hexagonal Ba$_{2-x}$Bi$_x$CoRuO$_6$ ($0.0 \le x \le 0.6$) perovskites are the promising thermoelectric oxides.

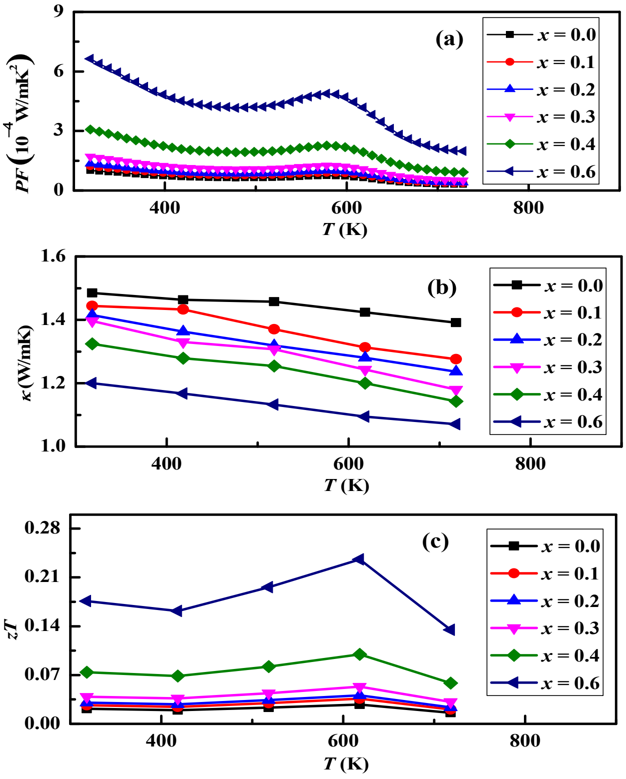

Figure 9 Temperature dependent thermoelectric power factor (*PF*) (a); thermal conductivity (κ) (b) and thermoelectric figure-of-merit (*zT*) (c) for Ba$_{2-x}$Bi$_x$CoRuO$_6$ ($0.0 \le x \le 0.6$) samples.

Table 5 Power factor (*PF*) and the dimensionless thermoelectric figure-of-merit (*zT*) of different double perovskite oxide materials.

Materials	***T/K***	**PF (σ·S^2) × 10^{-4} /Wm^{-1} K^{-2}**	***zT***	**Reference**
$Sr_{1.7}Ba_{0.3}FeMoO_6$	1100	0.8	-	54
Ca_2FeMoO_6	1200	3.5	-	55
$Sr_{1.6}K_{0.4}FeMoO_6$	1250	4.2	0.24	56
$Sr_{1.9}La_{0.1}MnMoO_6$	1250	1.2	0.13	57
Sr_2FeMoO_6	1000	1.2	0.05	58
$Ba_{0.15}Sr_{1.85}TiCoO_6$	1220	1.0	0.295	59
$Ba_{0.15}Sr_{1.85}Ti_{0.8}Fe_{0.8}Nb_{0.4}O_6$	923	0.13	-	60
Sr_2TiMoO_6	1223	0.11	-	61
Sr_2TiCoO_6	1150	0.065	-	62

3.3. Thermal conductivity

Fig. 9(b) shows thermal conductivity (κ) of $Ba_{2-x}Bi_xCoRuO_6$ ($0.0 \leq x \leq 0.6$) samples as a function of temperature. The κ values decrease with increasing temperature for all samples in the measured temperature range. Moreover, κ also decreases with increasing Bi doping. The κ values at 318 K and 618 K are listed for all samples in Table 4. The total thermal conductivity (κ) can be expresed by the sum of lattice thermal conductivity (κ_{Lat}) and electrical thermal conductivity (κ_{el}): [$\kappa = \kappa_{el} + \kappa_{Lat}$]. The κ_{el} can be calculated with the help of Wiedemann– Franz's law [$\kappa_{el} = LT/\rho$], where '*L*' is the Lorentz number and its value is ~ 2.44×10^{-8} W·Ω/K^2 for free electrons, *T* is the temperature and ρ is electrical resistivity.[63] Consequently, κ_{Lat} can be estimated from the expression: ($\kappa_{Lat} = \kappa - \kappa_{el}$). The lowering of κ with increasing Bi doping may be explained by two main factors: 1) due to increase in ρ which decreases κ_{el} as per the relation given above 2) due to the presence of lone pair of electrons on Bi^{3+} cations, which results in structural distortions and increase in the phonon scattering thereby lowering the κ_{Lat}.

3.4. Thermoelectric figure- of-merit (*zT*)

The dimensionless thermoelectric figure-of-merit (*zT*) for the $Ba_{2-x}Bi_xCoRuO_6$ ($0.0 \leq x \leq 0.6$) samples as a function of temperature are displayed in Fig. 9(c). The *zT* of all Bi-doped samples are higher than that of the undoped Ba_2CoRuO_6 compound. The $x = 0.6$ sample has the highest *zT* ~ 0.23 at 618 K, which is approximately 8 times higher than the pristine Ba_2CoRuO_6 compound. The increase in *zT* values for doped samples is due to the improved *S* and low κ of the studied samples. Thermoelectric figure- of-merit of all Bi-doped samples are reasonably high, as listed in Table 4. The *zT* for $x = 0.6$ sample is comparable or even better than the reported *zT* values for other cubic double perovskite oxide materials (See Table 5). It is the first time that we are reporting promising *p*-type thermoelectric properties of hexagonal double perovskite oxides and we anticipate that thermoelectric performance of these materials can be further improved by carrying out more comprehensive studies.

4. Conclusion

In conclusion, nontoxic and environment friendly high temperature thermoelectric $Ba_{2-x}Bi_xCoRuO_6$ ($0.0 \leq x \leq 0.6$) samples have been prepared with the traditional solid-state reaction method. The structural investigations with powder synchrotron X-ray and neutron diffraction reveal that these materials adopt the hexagonal 6H-perovskite structure with $P6_3/mmc$ space group. The crystallographic lattice parameters and unit cell volumes are found to increase with Bi doping, demonstrating that electronic effects (reduction of Co/Ru) dominate over steric effects and results in an expansion of unit cell, despite Bi^{3+} having a smaller ionic radius than Ba^{2+}.

SEM images depict that samples with higher doping levels have larger grain size. A substantial improvement in the Seebeck coefficient and reduction in thermal conductivity of Bi substituted samples have been observed. The highest power factor (*PF*) and thermoelectric figure-of-merit (*zT*) of ~6.6×10^{-4} W/m·K^2 and 0.23, respectively at 618 K are achieved for $x = 0.6$ sample, which is comparable or better than the many other published results for cubic double perovskite oxides. These findings show hexagonal double perovskites are potential TE materials and that Bi-doping is a useful way for improving the properties.

Acknowledgements

We are thankful to the Higher Education Commission (HEC) of Pakistan (Grant no.: 1981), and the British Council, United Kingdom for providing financial support to this research project. Synchrotron experiments were performed at the ALBA Synchrotron during U.H.'s three months stay granted by the OPEN SESAME fellowship training within Horizon 2020 project framework. Neutron powder diffraction data at ILL were performed through the EASY access program (EASY-320 proposal). U.H. is grateful to the Department of Energy Conversion and Storage, Technical University of Denmark (DTU) for supporting her research visit at DTU.

References

(1) Bell, L. E., Cooling, Heating, Generating Power, and Recovering Waste Heat with Thermoelectric Systems. *Science* **2008**, *321*, 1457–1461.

(2) Kim, H. S.; Liu, W.; Ren, Z., The bridge between the materials and devices of thermoelectric power generators. *Energy Environ. Sci*. **2017**, *10*, 69–85.

(3) Kanas, N.; Bjørk, R.; Wells, K. H.; Schuler, R.; Einarsrud, M. A.; Pryds, N.; & Wiik, K., Time-enhanced performance of oxide thermoelectric modules based on a hybrid *p-n* junction. *ACS Omega* **2021**, *6,* 197–205.

(4) Lu, X.; Morelli, D. T.; Xia, Y.; Ozolins, V., Increasing the Thermoelectric Figure of Merit of Tetrahedrites by Co-Doping with Nickel and Zinc. *Chem. Mater*. **2015**, *27*, 408–413.

(5) Fu, C.; Zhu, T.; Liu, Y.; Xie, H.; Zhao, X., Band engineering of high performance p-type FeNbSb based half-Heusler thermoelectric materials for figure of merit $zT > 1$. *Energy Environ. Sci*. **2015**, *8*, 216–220.

(6) He, Y.; Day, T.; Zhang, T.; Liu, H. Shi, X.; Chen, L.; Snyder, G. J., High Thermoelectric Performance in Non-Toxic Earth-Abundant Copper Sulfide. *Adv. Mater*. **2014**, *26*, 3974–3978.

(7) Paul, B.; Rawat, P. K.; Banerji, P., Dramatic enhancement of thermoelectric power factor in PbTe:Cr co-doped with iodine· *Appl. Phys. Lett.* **2011**, *98*, 262101.

(8) Pei, Y.; Shi, X.; Lalonde, A.; Wang, H.; Chen, L.; Snyder, G. J., Convergence of electronic bands for high performance bulk thermoelectrics. *Nature* **2011**, *473*, 66.

(9) Heremans, J. P.; Jovovic, V; Toberrer, E. S.; Saramat, A.; Kurosaki, K.; Charoenphakdee, A.; Yamanaka, S.; Snyder, G. J., Enhancement of thermoelectric efficiency in PbTe by distortion of the electronic density of states. *Science* **2008**, *321*, 554–557.

(10) Ning, H.; Mastrorillo, G. D.; Grasso, S.; Du, B.; Mori, T.; Hu, C.; Xu, Y.; Simpson, K.; Maizza, G.; Reece, M. J., Enhanced thermoelectric performance of porous magnesium tin

silicide prepared using pressure-less spark plasma sintering. *J. Mater. Chem. A* **2015**, *3*, 17426–17432.

(11) Terasaki, Y.; Sasago, K.; Uchinokura, K., Large thermoelectric power in $NaCo_2O_4$ single crystals. *Phys. Rev. B* **1997**, *56*, R12685–R12687.

(12) Ohtaki, M.; Tsubota, T.; Eguchi, K.; Arai, H., High-temperature thermoelectric properties of $(Zn_{1-x}Al_x)O$. *J. Appl. Phys.* **1996**, *79*, 1816–1818.

(13) Han, L.; Christensen, D. V.; Bhowmik, A.; Simonsen, S. B.; Le, T. H.; Abdellahi, E.; Chen, Y. Z.; Van Nong, N.; Linderoth, S.; Pryds, N., Scandium-doped zinc cadmium oxide as a new stable *n*-type oxide thermoelectric material. *J. Mater. Chem. A* **2016**, *4*, 12221–12231.

(14) Okuda, T.; Nakanishi, K.; Miyasaka, S.; Tokura, Y., Large thermoelectric response of metallic perovskites: $Sr1-xLaxTiO_3(0<\sim x<\sim 0.1)$. *Phys. Rev. B: Condens. Matter* **2001**, *63*, 113104.

(15) Ohta, S.; Nomura, T.; Ohta, H.; Koumoto, K., High-temperature carrier transport and thermoelectric properties of heavily La- or Nb-doped SrTiO3 single crystals. *J. Appl. Phys.* **2005**, *97*, 034106.

(16) Flahaut, D.; Mihara, T.; Funahashi, R.; Nabeshima, N.; Lee, K.; Ohta, H.; Koumoto, K., Thermoelectrical properties of A-site substituted $Ca_{1-x}Re_xMnO_3Ca_{1-x}Re_xMnO_3$ system. *J. Appl. Phys.* **2006**, *100*, 084911.

(17) Ohta, S.; Nomura, T.; Ohta, H.; Hirano, M.; Hosono, H.; Koumoto, K., High Temperature Thermoelectric Response of Electron-Doped $CaMnO_3$. *Appl. Phys. Lett.* **2005**, *87*, 1092108.

(18) Sugiura, K.; Ohta, H.; Nomura, K.; Hirano, M.; Hosono, H.; Koumoto, K., High electrical conductivity of layered cobalt oxide $Ca_3Co_4O_9$ epitaxial films grown by topotactic ion-exchange method. *Appl. Phys. Lett.* **2006**, *89*, 032111.

(19) Le, T. H.; Van Nong, N.; Snyder, G. J.; Viet, M. H.; Balke, B.; Han, L.; Stamate, E.; Linderoth, S.; Pryds, N., High performance *p*-type segmented leg of misfit-layered cobaltite and half-Heusler alloy. Energy Convers. Manag. **2015**, *99*, 20–27.

(20) Funahashi, F.; Matsubara, I.; Sodeoka, S., Thermoelectric properties of $Bi_2Sr_2Co_2O_x$ polycrystalline materials. *Appl. Phys. Lett.* **2000**, *76*, 2385.

(21) Kim, S.H.; Battle, P. D., Structural and Electronic Properties of the Mixed Co/Ru Perovskites $AA'CoRuO_6$ (A, A' = Sr, Ba, La). *J. Solid State Chem.* **1995**, *114*, 174−183.

(22) Bos, J-.W. G.; Attfield, J. P., Structural, Magnetic, and Transport Properties of $(La_{1+x}Sr_{1-x})CoRuO_6$ Double Perovskites. *Chem. Mater.* **2004**, *16*, 1822−1827.

(23) Burbank, R. D.; Evans H. T., The crystal structure of hexagonal barium titanate. *Acta Cryst.* **1948**, *1*, 330.

(24) Sher, F.; Attfield, J. P., Synthesis, Structure and Magnetic Properties of Ba_2CrMoO_6. *Solid State Sci.* **2006**, *8*, 277−279.

(25) Retuerto, M.; Alonso, J. A.; Martínez-Lope, M. J.; García-Hernández, M.; Krezhov, K.; Spirov, I.; Ruskov, T.; Fernández-Díaz, M. T., Crystal Structure and Magnetism of the 6H Hexagonal Double Perovskites Ba_2FeSbO_6 and $Ba_2CoSbO_{6-\delta}$: A Neutron Diffraction and Mössbauer Spectroscopy Study. *Eur. J. Inorg. Chem.* **2008**, 2286–2294.

(26) Ivanov, S. A.; Nordblad, P.; Mathieu, R.; Tellgren, R.; Ritter, C., Neutron diffraction studies and the magnetism of an ordered perovskite: Ba_2CoTeO_6. *Dalton Trans.* **2010**, *39*, 5490−5499.

(27) Kayser, P.; Injac, S.; Ranjbar, B.; Kennedy, B. J.; Avdeev, M.; Yamaura, K., Magnetic and structural studies of Sc containing ruthenate double perovskites A_2ScRuO_6 (A = Ba, Sr). *Inorg. Chem.* **2017**, *56*, 9009−9018.

(28) Bader, H.; Kemmler S. S., Ü ber Sauerstoffperowskite des fü nfwertigen Rutheniums $A_2B^{III}Ru^{V}O_6$ mit A = Ba, Sr. Z. *Anorg. Allg. Chem.* **1980**, *466*, 97–102.

(29) Parka, J. W.; Kwak, D. H.; Yoon, S. H.; Choi, S. C., Thermoelectric properties of Bi, Nb co-substituted $CaMnO_3$ at high temperature *J. Alloys Compd.* **2009**, *487*, 550–555.

(30) Kabir, R.; Tian, R.; Zhang, T.; Donelson, R.; Tan, T. T.; Li, S., Role of Bi doping in thermoelectric properties of $CaMnO_3$ *J. Alloys Compd.* **2015**, *628*, 347–351.

(31) Xu, G.; Funahashi, R.; Shikano, M.; Matsubara, I.; Zhou, Y., Thermoelectric properties of the Bi- and Na-substituted $Ca_3Co_4O_9$ system *Appl. Phys. Lett.* **2002**, *80*, 3760.

(32) Fauth, F.; Peral, I.; Popescu, C.; Knapp, M., The new material science powder diffraction beamline at ALBA synchrotron. *Powder Diffr.* **2013**, *28*, S360–S370.

(33) Peral, I.; Mckinlay, J.; Knapp, M.; Ferrer, S., Design and construction of multicrystal analyser detectors using Rowland circles: application to MAD26 at ALBA. *J. Synchrotron Radiat.* **2011**, *18*, 842–850.

(34) Toby, B. H., EXPUGUI, a graphical user interface for GSAS. *J. Appl. Crystallogr.* **2001**, *34*, 210–213.

(35) Momma, K.; Izumi, F. VESTA 3 for three-dimensional visualization of crystal, volumetric and morphology data. *J. Appl. Crystallogr.* **2011**, *44*, 1272−1276.

(36) Howard, C. J., The approximation of asymmetric neutron powder diffraction peaks by sums of Gaussians. *J. Appl. Crystallogr.* **1982**, *15*, 615–620.

(37) Ferreira, T.; Morrison, G.; Yeon, J.; Loye, H-C. Z., Design and Crystal Growth of Magnetic Double Perovskite Iridates: Ln_2MIrO_6 (Ln = La, Pr, Nd, Sm-Gd; M = Mg, Ni). *Cryst. Growth Des.* **2016**, *16*, 2795−2803.

(38) Sher, F.; Venimadhav, A.; Blamire, M. G.; Dabrowski, B.; Kolesnik, S.; Attfield, J. P., Structural, magnetic and transport properties of $Sr_2Fe_{1-x}Mg_xMoO_6$ ($0 \leq x \leq 1$) double perovskites. *Solid State Sci.* **2005**, *7*, 912−919.

(39) Dorai, A. K.; Masuda, Y.; Joo, J. H.; Woo, S. K.; Kim, S. D., Influence of Fe doping on the electrical properties of $Sr_2MgMoO_{6-\delta}$. *Mater. Chem. Phys.* **2013**, *139*, 360-363.

(40) Vilesh, V. L.; Subodh, G., Crystal structure and dielectric properties of $BaANaTeO_6$ (A = Bi, La) double perovskites. *Ceram. Int.* **2017**, *43*, 12718−12723.

(41) Warren, B. E. X-ray Diffraction; Dover Publications: New York, **1990**.

(42) Liu, Y.; Lin, Y.; Jiang, L.; Nan, C. W.; Shen, Z., Thermoelectric properties of Bi^{3+} substituted Co-based misfit-layered oxides. *J. Electroceram.* **2008**, *21*, 748–751.

(43) Wanga, D.; Chena, L.; Yaoa, Q.; Lib, J., High-temperature thermoelectric properties of $Ca_3Co_4O_{9+\delta}$ with Eu substitution. *Solid State Commun.* **2004**, *129*, 615–618.

(44) Seshadri, R.; Hill, N. A., Visualizing the Role of Bi 6s “Lone Pairs” in the Off-Center Distortion in Ferromagnetic $BiMnO_3$. *Chem. Mater.* **2001**, *1*3, 2892−2899.

(45) Lee. S. B.; Chen, R.; Balents, L., Metal-insulator transition in a two-band model for the perovskite nickelates. *Phys. Rev. B* **2011**, *84*, 165119.

(46) Saxena, M.; Tanwar, K.; Maiti, M., Environmental friendly Sr_2TiMoO_6 double perovskite for high temperature thermoelectric applications *Scripta Materialia* **2017**, *130*, 205–209.

(47) N.F.; Mott, E.A., Davis, Electronic Processes in Non-Crystalline Materials. Clarendon Press, Oxford, 1971.

(48) Kharrat. A. B. J.; Moussa. S.; Moutiaa. N.; Khirouni. K.; Boujelben, W., Structural, electrical and dielectric properties of Bi-doped $Pr_{0.8-x}Bi_xSr_{0.2}MnO_3$ manganite oxides prepared by sol-gel process. *J. Alloys Comp.* **2017**, *724*, 389−399.

(49) Sugahara, T.; Ohtaki, M., Structural and semiconductor-to-metal transitions of double-perovskite cobalt oxide $Sr_{2-x}La_xCoTiO_{6-\delta}$ with enhanced thermoelectric capability *Appl. Phys. Lett.* **2001**, *99*, 062107-1–062107-3.

(50) Sugahara, T.; Ohtaki, M.; Suganuma, K., La doped effects on structure and thermoelectric properties of Sr_2MnMoO_6 double-perovskite oxides. *J. Asian Ceram. Soc.* **2013**, *1*, 282–288.

(51) Roy, P.; Waghmare, V.; Maiti, T., Environmentally friendly $Ba_xSr_{2-x}TiFeO_6$ double perovskite with enhanced thermopower for high temperature thermoelectric power generation. *RSC Adv.* **2016**, *6*, 54636–54643.

(52) Jaime, M.; Salamon, M. B.; Rubinstein, M.; Treece, R. E.; Horwitz, J. S.; Chrisey, D. B., High-temperature Thermopower in $La_{2/3}Ca_{1/3}MnO_3$ Films: Evidence for Polaronic Transport. *Phys. Rev. B* **1996**, *54*, 11914−11917.

(53) Huang, X. Y.; Miyazaki, Y.; Kajitani, T., High temperature thermoelectric properties of $Ca_{1-x}Bi_xMn_{1-y}V_yO_{3-\delta}$ ($0 \le x = y \le 0.08$). *Solid State Commun.* **2008**, *145*,132–136.

(54) Sugahara, T.; Ohtaki, M.; Souma, T., Thermoelectric properties of double-perovskite oxide $Sr_{2-x}M_xFeMoO_6$ (M = Ba, La). *J. Ceram. Soc. Japan.* **2008**, *116*, 1278–1282.

(55) Sugahara, T.; Nong, N. V.; Ohtaki, M., Structure and thermoelectric properties of $Ca_{2-x}Sr_xFeMoO_6$ ($0 \le x \le 0.3$) double-perovskite oxides. *Mater. Chem. Phys.* **2012**, *133*, 630–634.

(56) Sugahara, T.; Araki, T.; Ohtaki, M.; Suganuma, K., Structure and thermoelectric properties of double-perovskite oxides: $Sr_{2-x}K_xFeMoO_6$. J. *Ceram. Soc. Japan* **2012**, *120*, 211–216.

(57) Sugahara, T.; Ohtaki, M.; Suganuma, K., La doped effects on structure and thermoelectric properties of Sr_2MnMoO_6 double-perovskite oxides. *J. Asian Ceram. Soc.* **2013**, *1*, 282–288.

(58) Popuri, S. R.; Redpath, D.; Chan, G.; Smith, R. I.; Cespedes, O.; Bos, J-W. G., Antisite-disorder, magnetic and thermoelectric properties of Mo-rich $Sr_2Fe_{1-y}Mo_{1+y}O_6$ ($0 \leq y \leq 0.2$) double perovskites. *Dalton Trans*. **2015**, *44*, 10621–10627.

(59) Saxena, M.; Roy, P.; Acharya, M.; Bose, I.; Tanwar, K.; Maiti, T., Enhanced thermoelectric figure-of-merit in environmentally benign $Ba_xSr_{2-x}TiCoO_6$ double perovskites. *Appl. Phys. Lett.* **2016**, *109*, 263903-1–263903-1.

(60) Roy, P.; Waghmare, V.; Tanwar, K.; Maiti, T., Large change in thermopower with temperature driven *p–n* type conduction switching in environment friendly $Ba_xSr_{2x}Ti_{0.8}Fe_{0.8}Nb_{0.4}O_6$ double perovskites. *Phys. Chem. Chem. Phys.* **2017**, *19*, 5818–5829.

(61) Saxena, M.; Tanwar, K.; Maiti, M., Environmental friendly Sr_2TiMoO_6 double perovskite for high temperature thermoelectric applications *Scripta Materialia* **2017**, *130*, 205–209.

(62) Saxena, M.; Maiti, T., Compositional modification of Sr_2TiCoO_6 double perovskites by Mo and La for high temperature thermoelectric applications *Ceram. Int.* **2018**, *44*, 2732–2737.

(63) Snyder, G. J.; Toberer, E. S., Complex thermoelectric materials. *Nat. Mater.* **2008**, *7*, 105–114.

For Table of Contents Only

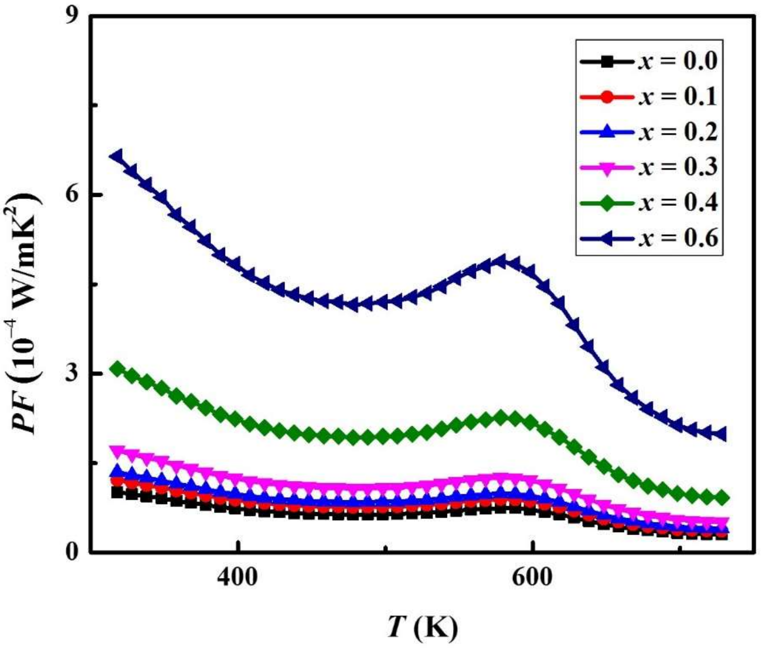

Chemically doped $Ba_{2-x}Bi_xCoRuO_6$ hexagonal double perovskite-type oxides were prepared using the conventional solid-state chemistry method. Interesting *p*-type thermoelectric properties were observed in all samples. Simultaneous enhancement of the power factor and reduction of thermal conductivity was achieved, thus improving the figure-of-merit (zT) to ~0.23 for $x = 0.6$